A Silicon Synapse

James Jeanne, Joanna Thomas, Teddy Yu

The University of California, San Diego
BGGN 260 Neurodynamics
Dr. Gert Cauwenberghs

Submitted 3/22/2007

The term 'neuromorphic engineering' was coined by Carver Mead almost 20 years ago (Mead, 1990) but neuromorphic engineering has been in the making since integrated circuits first came into existence. Once engineers were able to implement mathematical models in silicon, silicon neurons based on a variety of mathematical models for neuron behavior became a research focus. The Hodgkin-Huxley (HH) model of a squid giant axon is arguably the most well known mathematical model of neuron firing; however, design and fabrication of a bank of HH neurons, each with 6 parameters, consumes valuable space on a chip, and is not straightforward to implement. Integrate and fire (IF) silicon neurons are a less complicated alternative to HH neurons since they do not model the opening and closing of ion channels. Rather, they simply accumulate charge on the membrane and produce a spike when the membrane voltage reaches a threshold value. The objective of this project was to design and simulate a coupled neuron pair using an IF neuron model and a conductance based synapse.

The synapse was designed to implement a standard conductance-based model, while the IF neuron was designed to emulate the biological signal. The simulated synapse to neuron connection successfully produced biologically realistic spikes in the postsynaptic neuron. A cascade of two synapses interposed with two neurons also produced spikes at each neuron. However, the spike width decreased as the spike propagated along the synapses, an issue that would need to be addressed in implementations of longer chains of synaptically-coupled neurons.

Introduction

Hodgkin-Huxley model

The most widely used mathematical model of a neuron, the Hodgkin-Huxley (HH) model, was published in 1952 based on studies of a squid giant axon. The work earned Hodgkin and Huxley a shared Nobel Prize in physiology and medicine in 1963. The squid giant axon was chosen as the study subject for its size; working on an axon ~1mm in diameter was much more accessible than human neurons. Hodgkin and Huxley determined that membrane action potential generation can be described by electric circuits and voltage-dependent conductances of ion channels, more specifically sodium and potassium channels (figure 1).

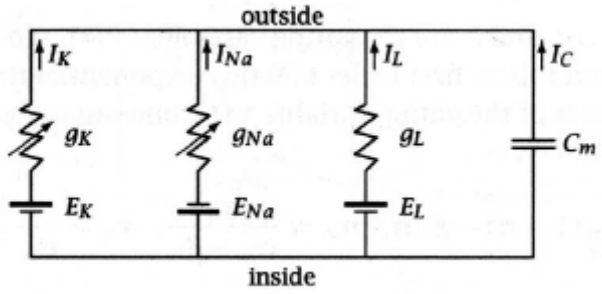

Figure 1. Circuit schematic of the elements in the Hodgkin-Huxley model of the squid giant axon

The equations that represent the circuit above are given below (equations 1-4). A leak current is incorporated into the calculations in addition to the sodium and potassium ion channel currents. With four variables (V, n, m, and h) and six parameters (an α, and β for n, m, and h respectively) the equations are complex; however, n, m, and h are only affected by cell potential, V.

$$\frac{dV}{dt} = \left(\frac{I_{ext} - \bar{g}_k n^4 (V_m - E_k) - \bar{g}_{Na} m^3 h (V_m - E_{Na}) - g_L (V_m - E_L)}{C} \right) \quad (1)$$

$$\frac{dn}{dt} = \alpha_n (1 - n) - \beta_n n \quad (2)$$

$$\frac{dm}{dt} = \alpha_m (1 - m) - \beta_m m \quad (3)$$

$$\frac{dh}{dt} = \alpha_h (1 - h) - \beta_h h \quad (4)$$

Equations 1-4. Hodgkin-Huxley equations to model the behavior of the squid giant axon. See BGGN260 class notes for definitions of α and β.

As expected of a model that quantitatively represents neuron behavior the HH model produces an accurate action potential and a refractory period post-action potential that impacts electrical properties (Abbott and Kepler, 1990). While the HH equations model channel activation and inactivation as kinetically independent, and estimates a short time to the first open channel (Destexe et al., 1994), the model accurately represents macroscopic currents.

Morris-Lecar model

In 1981 Morris and Lecar published a modified set of Hodgkin-Huxley equations that represented neuron behavior in barnacle giant muscle fibers (BGMF) (equations 5-7).

$$\frac{dV}{dt} = I_{ext} - g_L V_L - g_{Ca} M (V - V_{Ca}) - g_k N (V - V_K) \quad (5)$$

$$\frac{dM}{dt} = \lambda_m V [M_\infty V - M] \quad (6)$$

$$\frac{dN}{dt} = \lambda_N V [N_\infty V - N] \quad (7)$$

Prior to 1981, studies on the BGMF indicated voltage dependent Ca^{2+} and K^+ channels, which were rarely inactive, comprised the membrane conductance system (Morris and Lecar, 1981). However, the voltage behavior of the BGMF proved more complex. Morris and Lecar questioned if a system of just two non-inactivating conductances could adequately represent the oscillatory voltage behavior of the BGMF. They feared their system would not be able to account for other complicating factors such as ion accumulation, slow inactivation, and inhomogeneous distribution of channel types. For their simple model they assigned two independent voltage-dependent conductances (g_k and g_{Ca}) and assumed the relaxation kinetics were first order. They also used linear relations for the instantaneous current-voltage curves through open channels, ignoring the deviation from linearity that occurs under high permeable-ion gradient. In spite of their concerns, what became known as the Morris-Lecar model of a neuron performed well quantitatively when compared to current-clamp data. The system was capable of two modes of oscillation, damped and limit cycle (see figure 2), but did have limitations. Generating oscillations that begin small and grow or a bistable oscillation pattern were beyond the scope of the model.

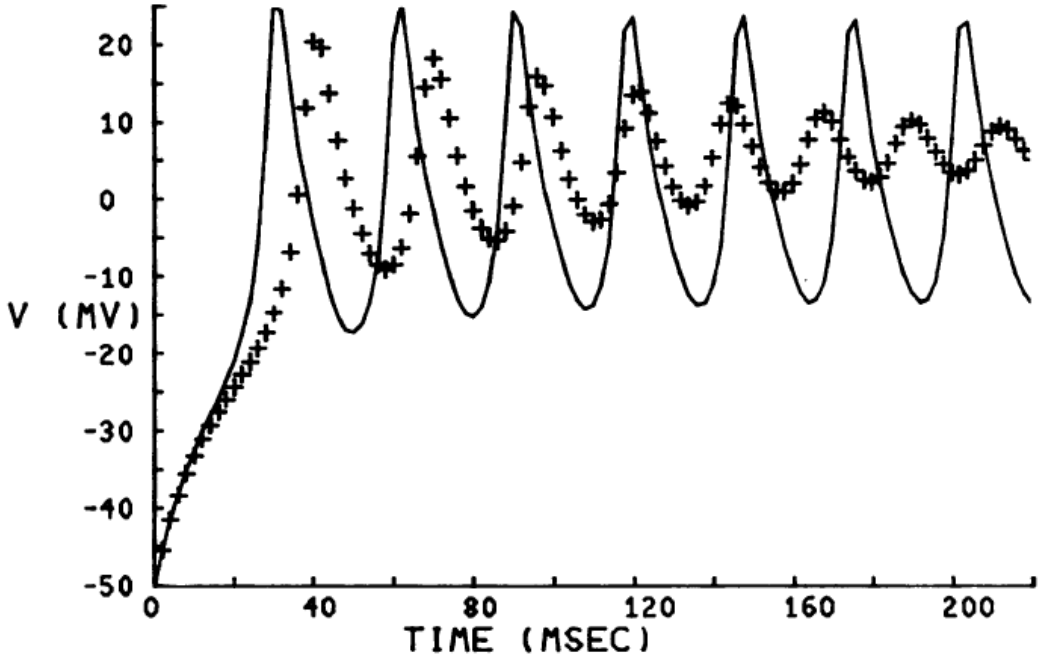

Figure 2. Examples of output limit-cycle oscillations generated with the Morris-Lecar third-order system

Markov model

Markov models or Markov chains were first proposed for the study of discrete-time stochastic processes by Russian mathematician Andrey Markov in 1906. They have since been employed to study a broad spectrum of topics ranging from games of chance such as Candyland to algorithmic music composition. In 1966, Katz used a set of simple Markovian equations to describe currents at the neuromuscular junction (Destexe et al., 1994). The state diagram (figure 3) and equations (equation 8 and 9) given below were generated by Vandenberg and Bezanilla (1991) to describe the squid giant axon while accounting for both open and closed channels and activation and deactivation of channels. In equation 8 for the model ionic current per channel, V is membrane potential in mV, γ_{Na} is the limiting single channel conductance, V_{Na} is the sodium reversal potential, and O is the number of open channels. Equation 9 is the Vandenberg-Bezanilla model gating current per channel where a, b, c, d, f, g, i, j, u, y, and z are rates (see Vandenberg and Bezanilla, 1991 for equations), O is the number of open channels, and $C_1 – C_5$, I, I_4, and I_5 are the probabilities of being in corresponding states

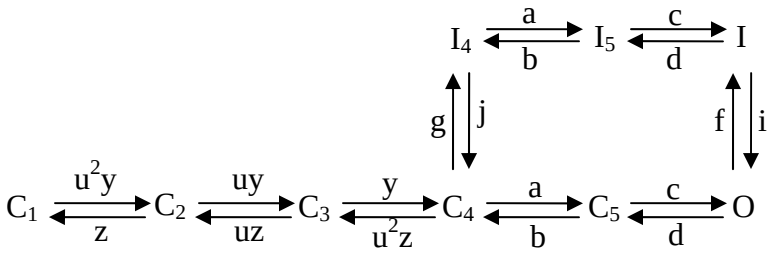

Figure 3. Markovian kinetics state diagram of the Vandenberg-Bezanilla expanded/detail sodium channel model.

$$i_{Na} = \gamma_{Na} V \frac{\exp\left[\left(V - V_{Na}\right)/24\right] - 1}{\exp\left(V/24\right) - 1} O \qquad (8)$$

$$i_g = 1.6x10^{-19} \begin{Bmatrix} 1.5\left[y\left(C_1 + C_2 + C_3\right) - z\left(C_2 + C_3 + C_4\right)\right] + .42\left(aC_4 - bC_5\right) \\ + 1.91\left(cC_5 + cI_5 - dO - dI\right) + .91\left(fO + gC_4 - iI - jI_4\right) \end{Bmatrix} \qquad (9)$$

Destexhe, *et. al.* (1994) compared the Vandenberg-Bezanilla detailed sodium channel model to a very simple Markovian sodium channel model and the Hodgkin-Huxley model and confirmed the following: a Markov model of neuron behavior can accurately convey both single channel events and cellular events, kinetic Markov models can describe enzymes and molecular interactions within a signaling nerve cell in addition to ion channel activity, and the state diagrams of Markov models are inherently adjustable so the models can be rapidly adapted as scientists better understand the molecules involved in a firing neuron (Destexhe, et al., 1994). More specifically they found the simple Markovian model to better represent single channel behavior due to its long predicted lag time to first channel openings. When modeling neuron behavior at the macroscopic level all three models evaluated performed acceptably (see figure 4).

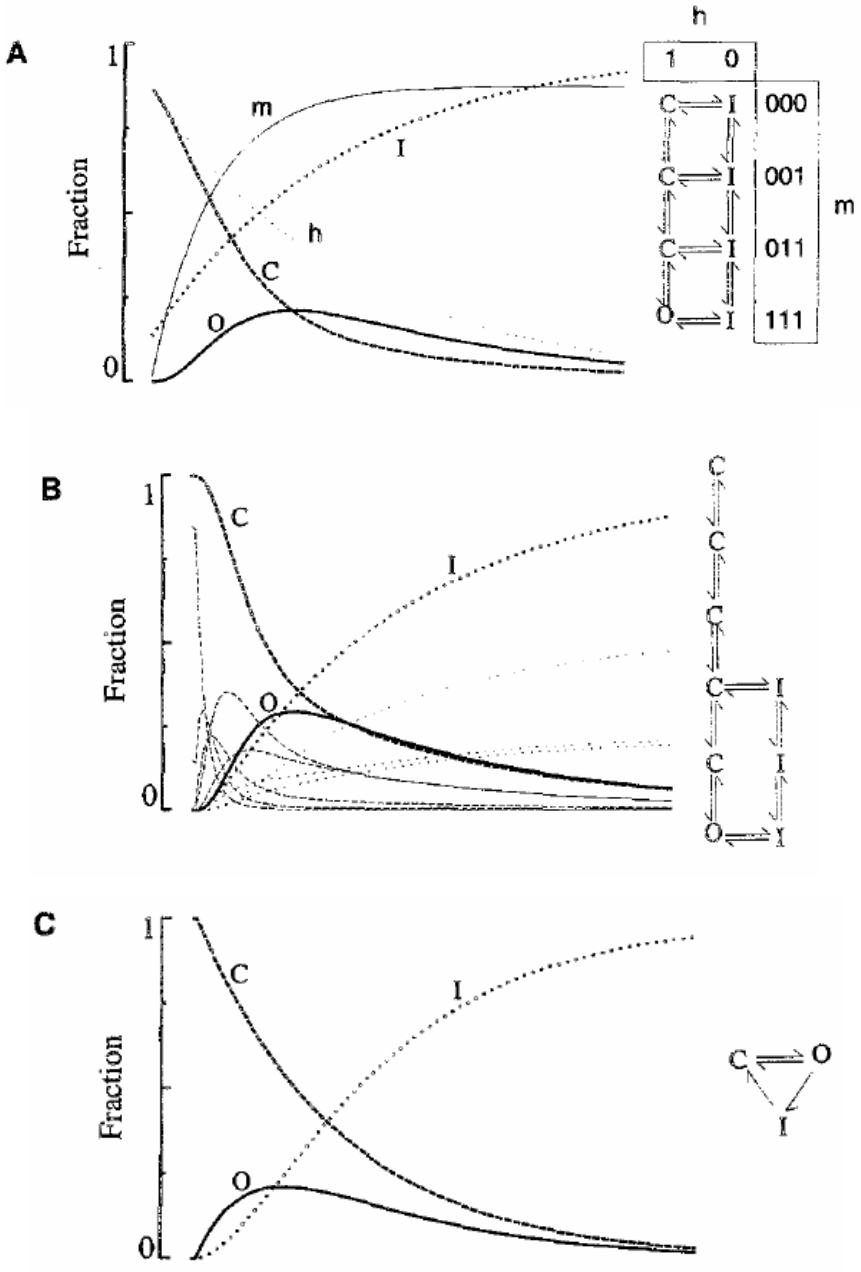

Figure 4. Outputs from the three kinetic models of a giant squid axon. O is the fraction of channels in the open state, C is the fraction of channels closed, and I is the fraction of channels in the inactivated state. A) A Markov scheme for the Hodgkin-Huxley model, B) the detailed Markov model from Vandenberg and Bezanilla, C) a simple three-state Markov model of the Vandenberg and Bezanilla version

VLSI

The same year the Hodgkin-Huxley model of the squid giant axon was published, the concept of the integrated circuit (IC) was published. Not long after, in 1959, the first IC circuits were successfully implemented, and by the 1980's, very large scale integrated (VLSI) circuits were the backbone of the modern computer. The similar conductivity across membranes and conductivity across silicon devices made the VLSI circuit a good candidate for replicating biological membrane conductance (Mahowald and Douglas, 1991). Research has shown VLSI neurons efficiently represent their biological counterparts (Mahowald and Douglas, 1991; Harrison and Koch, 1999, Le Masson et al., 1999) for three main reasons: they operate in real-time, they consume relatively little power, and they occupy a small area. To date networks of silicon neurons have been used to reproduce a variety of biological functions such as vision, hearing, and locomotion (Harrison and Koch, 1999; Horiuchi et al., 1992; Kameda and Yagi, 2003; Koch et al., 1991; Lewis and Simo, 1999; Lewis and Bekey, 2002; Tenore et al., 2004; Van Schaik and Shamma, 2004, Vogelstein et al., 2007).

Researchers have used VLSI to simulate invertebrate (fly) and vertebrate (primate) vision (Harrison and Koch, 1999; Kameda and Yagi, 2003). Both designs are targeted for use in robotics. Vision (or motion sensing) is an inherently more complex task than hearing due to the multiple, time-varying input signals (basic hearing has two time-varying signals). The fly-vision based sensor (FBS) processes information from multiple pixels in parallel rather than one pixel at a time; in order to navigate, the circuit computes directional information on the time scale of seconds (Harrison and Koch, 1999). Resolution remains the FBS's primary drawback. A typical CCD imager has a resolution of 640 x 480 pixels, while the FBS has a resolution up to 90 x 90 pixels; however, 90 x 90 pixels resolution is equivalent to some species of flies.

The vertebrate retina contains neurons that respond in various ways to light stimulation. Kameda and Yagi (2003) aimed to generate a silicon neuromorphic retina capable of mimicking both the sustained-type response during illumination and the transient-type response when light is switched on or off seen in vertebrate retinal neurons. Their silicon retina could detect movement on the time scale of milliseconds and with much lower resolution (40 x 46 pixels vs 640 x 480 pixels for a CCD) was able to produce a recognizable image (see figure 5) (Kameda and Yagi, 2003).

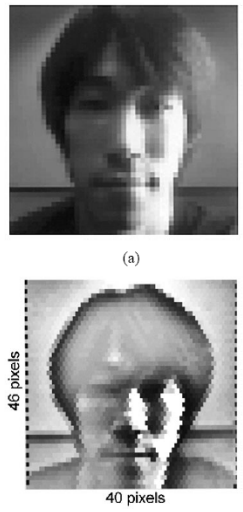

Figure 5. Comparison between output images of a CCD camera and the silicon retina. a) CCD camera, b) silicon retina. (Kameda and Yagi, 2003)

Researchers have been working for nearly two decades to implement cochlear functions in VLSI (Lyon and Mead, 1988) and the 'fly on the wall' has come a long way in 20 years. Today voice recognition and speech processing technology are commonplace. The primate cochlear basilar membrane can be modeled as a bank of frequency selective filters (Kumar et al., 1998); in figure 6, taken from Schaik, et al. 1998, each 'Cochlear Section' represents a frequency filter. Sounds that pass through the basilar membrane or signals that pass through the silicon filters result in either unique nerve firing patterns or set of zero-crossing events that, if processed correctly, can convey the same information contained in the nerve firing patterns (Fragniere et al., 1997). 'Silicon cochlea' can also be used to identify the position of the sound source (Van Shaik and Shamma, 2004). Based on the fact that humans utilize 'Interaural Time Difference' to locate a sound in a horizontal plane, Van Shaik and Shamma designed a sound localizer utilizing silicon cochlea that can detect sounds up to 300Hz within 3^{o} of their position.

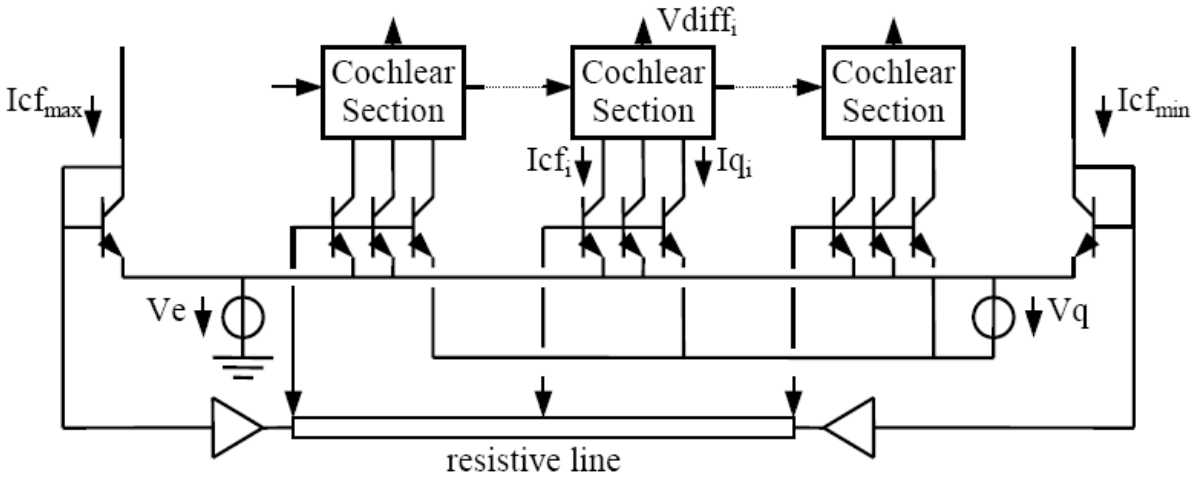

Figure 6. A silicon cochlea (Schaik et al., 1998)

A set of neural circuits found in the spinal column, known as the central pattern generator (CPG), is responsible for producing the oscillatory, periodic waveforms that stimulate muscles and in turn results in locomotion. Tenore et al. (2004) developed a VLSI chip for use in robots that generates oscillatory signals of different frequencies and phases and then synchronizes the signals by coupling integrate and fire (IF) neurons. A given phase difference between oscillatory signals, governed by the neurons, results in gait-like movement of the robot's limbs. The neuron model employed on the VLSI CPG emulator chip was less detailed than the HH or Morris-Lecar models; however, the numerous neurons on the chip were highly versatile, i.e. they could be used as continuous or spiking neurons. Also, the main synapses were dynamic in that they could be programmed as excitatory or inhibitory and sensory in that they could receive external signals; meanwhile, 10 feedback synapses were included on the chip that interconnected the neurons (Tenore et al., 2004).

In 1997 a patent for the 'silicon neuron' was issued to Douglas and Muhowald; since then, analogue circuitry designed to mimic one or many neurons firing has improved greatly. A key issue that often factors into a neuromorphic design is neuron coupling; beyond incorporating all the parameters needed to model an individual neuron spike, for an accurate representation of a neural network, the neurons must be coupled. Thus, for our BGGN260 term project we elected to research, design, and simulate a coupled pair of neurons. In lieu of building on the ground work laid by Larson, Matthews, and Aimone for the implementation of a Hodgkin-Huxley neuron in VLSI, due to concerns over understanding and modifying their detailed work in a short

time frame, our goal was the successful design and simulation of a coupled neuron pair using a simpler integrate and fire neuron model and a synapse modeled as a synaptic current.

Implementation

Integrate and fire neuron

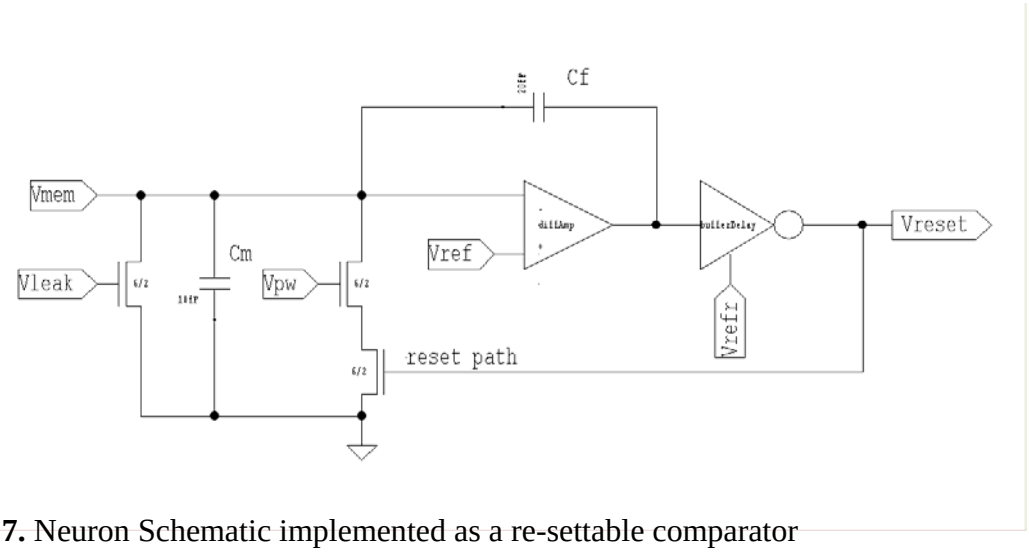

Figure 7. Neuron Schematic implemented as a re-settable comparator

The neuron is implemented using an integrate-and-fire model with a differential amplifier and reset circuitry. C_m, the membrane capacitor at the input to the differential amplifier, performs the integration. The value of C_m affects how easily the neuron integrates charge and the output spike amplitude; for instance, a larger C_m value would result in slower charging of the capacitor for each input pulse (due to the larger time constant) and a decrease in the output spike amplitude. A transistor from the input node to ground, fixed at a constant current with a bias voltage, generates the leak current.

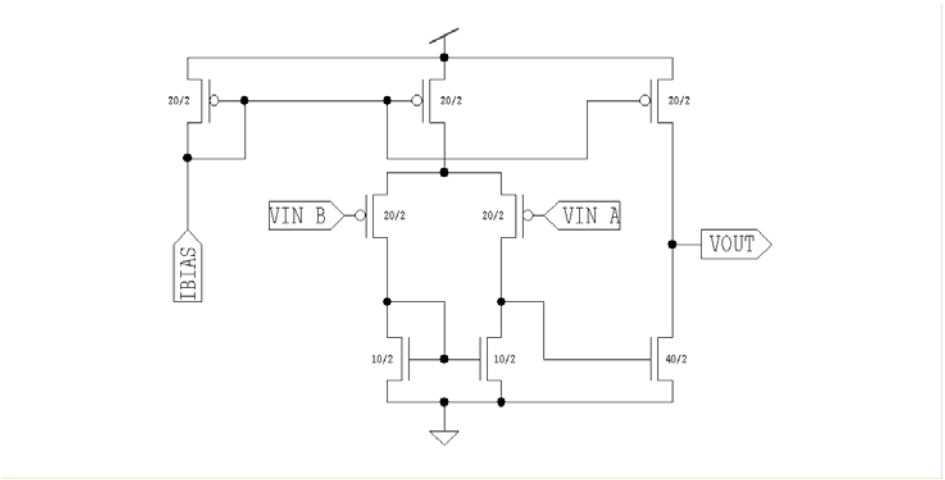

Figure 8. Differential Amplifier.

The differential amplifier consists of two gain stages: a PMOS first stage that increases dynamic input range for lower input voltage values and a second stage with a single-ended output. The W/L ratios in the PMOS and NMOS transistors are sized to 2:1 to compensate for the transistors' mobility values and maintain equal drain current values.

$I_d = [\mu*(C_{ox}/2)*(W/L)*((V_{gs}-V_{th})^2)]$ (active region).

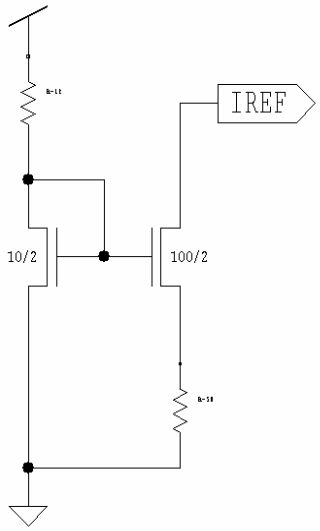

Figure 9. Widlar current source.

A bias current of ~ 1 mA was used in the differential amplifier. This is implemented with a simple Widlar current source. In the future, this can be replaced by more sophisticated bias circuits that are source voltage, process, or temperature independent.

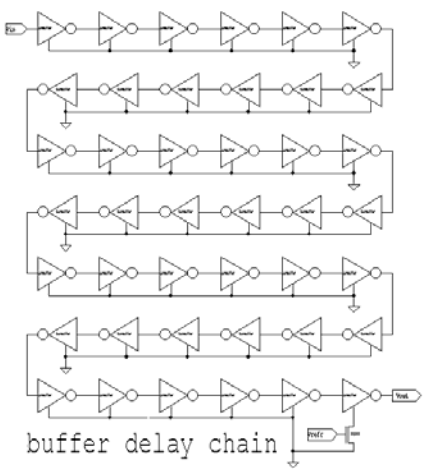

Figure 10. Buffer delay chain.

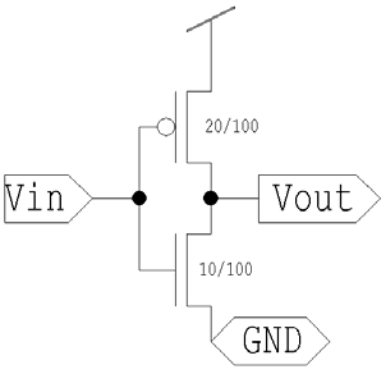

Figure 11. Low W/L ratio Inverters used in the Buffer delay chain.

A buffer stage (upper figure), consisting of cascaded inverters (lower figure) with small W/L ratios, follows the differential amplifier. The buffer stage has an additional current control (V_{refr}) that connects the NMOS of the previous inverter stage to ground, in the form of a transistor. Varying the input voltage to this transistor controls the maximum current flow at the

output. Capacitive feedback is employed by inserting a capacitor from the output of the differential amplifier to the input of the differential amplifier.

The on/off reset path consists of a single transistor connected from the input node to ground and controlled by the output node. Similar to the current control design in the buffer stage, a transistor was added in between the reset transistor and the input node to control the maximum current flow at the input.

The properties of the neuron spiking behavior that we are most interested in are: spike rise time, spike fall time, spiking amplitude, spiking frequency, and spike width. The spike rise time consists of two regimes: integration of charges upon the membrane capacitance C_m and the spike waveform once the threshold voltage is reached. The change in voltage at the membrane is governed by: $dV_m/dt = I/C_m$. It can easily be seen that the charge integration time at the membrane is directly proportional to the amplitude and frequency of incoming current and inversely proportional to the magnitude of C_m. The spike waveform rise time is governed by the slew rate of the amplifier which is similarly expressed as: $dV_{out}/dt = I/C_{out}$. Since I_d is proportional to transistor sizes, large W/L ratios in the output stage of the differential amplifier were chosen for adequate slew rate.

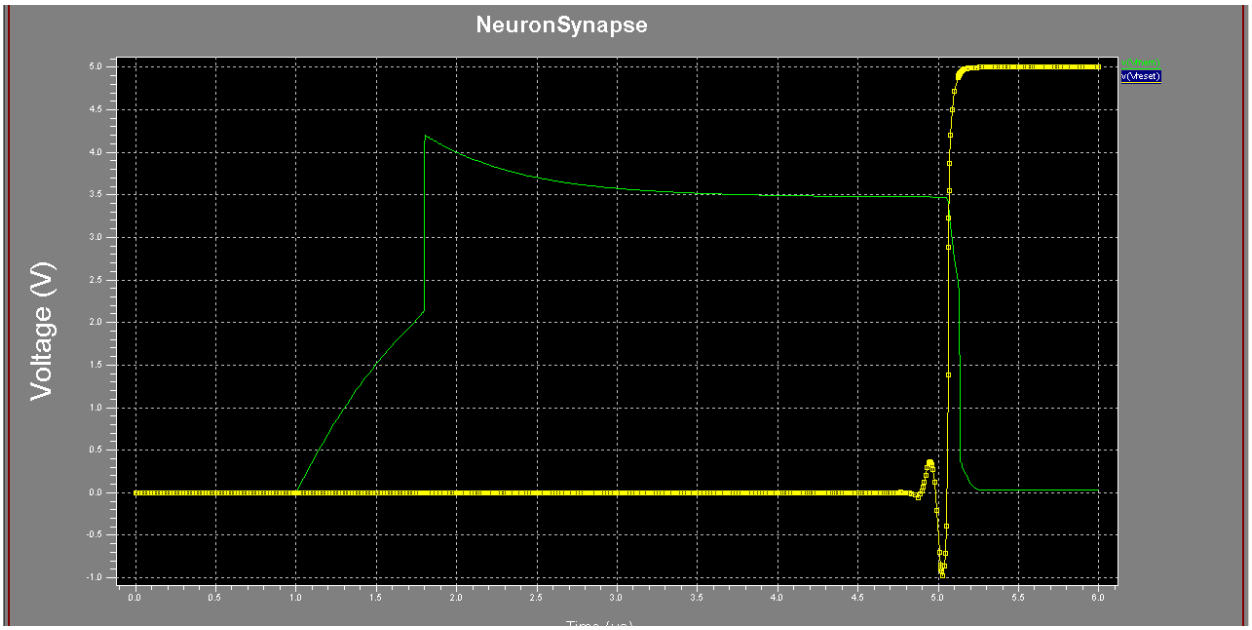

Figure 12. Neuron Spike detail: the initial decay is due to the leakage current, the slope of the secondary portion is controlled by V_{refr}, and the slope of the final portion is controlled by V_{pw}.

Similarly, the limit of the spike fall time is also governed by the slew rate equations with the current limiting transistors letting us dictate the shape. The top declining portion is due to the leakage current. The reset circuitry activates after the buffer delay as indicated in the figure above where the yellow waveform rises high. The current limiting transistor (V_{refr}) in the buffer stage governs the initial downward slope of the pulse while the current limiting transistor (V_{pw}) in the reset path governs the bottom portion of the pulse. Decreasing V_{ref} and V_{pw} will decrease the slope of the falling spike at each of these respective portions.

The spiking amplitude is primarily controlled by the ratio of the membrane capacitance Cm and the feedback capacitance C_f. These capacitors form a capacitive voltage divider where $V_{mem} = C_f/(C_m+C_f)*V_{out}$.

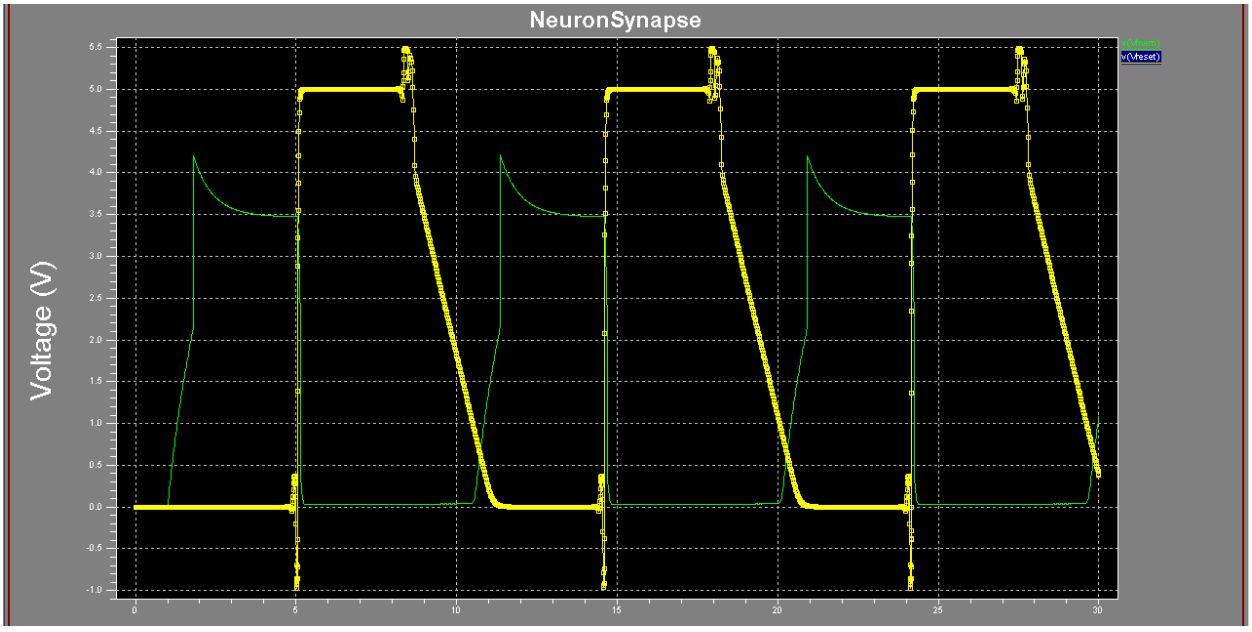

Figure 13. Neuron spike pulse train with the Vreset waveforms showing how the neuron spikes are suppressed while Vreset is higher than $V_{th0,n}$.

The spike frequency is primarily controlled by the decay time of the reset voltage V_{reset}, which is controlled by the current limiters V_{refr} and V_{pw}. The spike width also enforces a mandatory delay between spikes through the inherent delay in the V_{reset} pulse. The spike width is simply controlled by varying the delay of the buffer circuitry.

Conductance-Based Synapse

The model of synaptic transmission that we implemented is a standard conductance-based model that is discussed in detail in Destexhe, *et. al.* (1994). In particular, the model synapse used a Markov Model description to describe opening and closing dynamics with a closing rate that was dependent on the presynaptic neurotransmitter concentration, which was in turn dependent on the presynaptic voltage. Thus, the full synapse model is

$$I_{syn} = g_{syn} r(V_m - E_{syn}) \tag{10}$$

where r is a state variable describing the proportion of channels that are open, g_{syn} is the maximal conductance of the synapse, E_{syn} is the synaptic reversal potential, and V_m is the postsynaptic membrane voltage. Note that r evolves in time according to the differential equation

$$\frac{dr}{dt} = \alpha[T](V)(1-r) - \beta r. \tag{11}$$

Here, α[T](V) and β are transition rates of the channels from closed to open and open to closed, respectively. [T](V) is the neurotransmitter concentration, which has the following presynaptic voltage dependence:

$$[T] = \frac{[T]_{\max}}{1 + e^{-(V_{pre} - V_p)/k_p}}. \tag{12}$$

Design

The design of the synapse in analog VLSI circuitry will be described from the “output” (postsynaptic side) to the “input” (presynaptic side). To model the difference between the membrane voltage and the synaptic reversal potential in the postsynaptic cell, we used an operational transconductance amplifier (OTA) (Liu, *et. al* 2002) (See figure 14) and exploited the

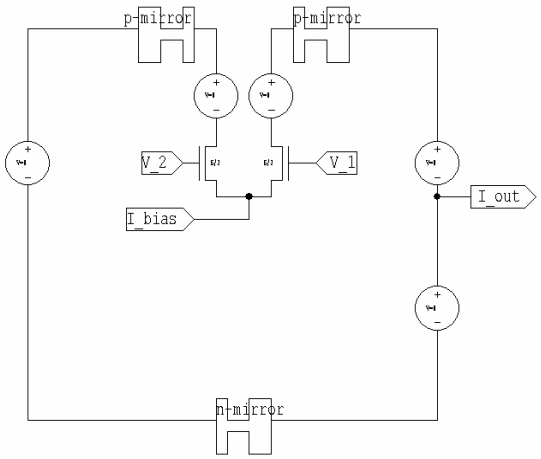

Figure 14. OTA with wide output range.

fact that the OTA's output current is almost mathematically identical to that of the empirical synapse model. When the OTA is operated below threshold, its output current is given by

$$I_{out} = I_b \tanh\left(\frac{\kappa_n}{2U_T}(V_1 - V_2)\right). \tag{13}$$

For small signals near $V_1 = V_2$, the tanh function can be approximated by its argument, yielding

$$I_{out} = \frac{I_b \kappa_n}{2U_T}(V_1 - V_2). \tag{14}$$

We then bias the V_2 input to E_{syn}, and simply require the bias current I_b to represent $g_{syn}r$. If the OTA is connected as a follower-integrator (see figure 15),

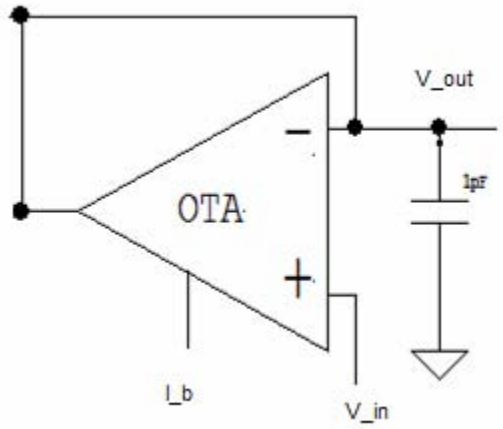

Figure 15. OTA connected as a Follower-Integrator.

then the postsynaptic voltage can be measured off the capacitor (*i.e.* at V_{out}) in the follower-integrator:

$$C\frac{dv}{dt}V_{out} = \frac{I_b\kappa_n}{2U_T}\left(V_{in} - V_{out}\right). \tag{15}$$

The dynamics of the gating variable, r, were implemented using two OTA follower-integrators with a common integration capacitor (see figure 16).

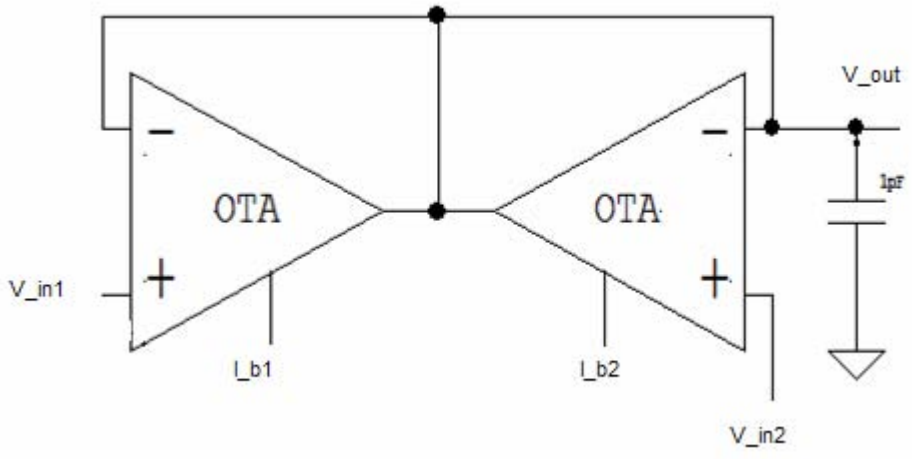

Figure 16. Two OTAs connected as Integrator-Followers with shared integration capacitor.

Each OTA represents one of the terms from the above equation. Because r is by definition restricted to the range of values from 0 to 1, voltage rails need to be added to the circuit. This is done by simply applying minimum and maxixmum bias voltages to the positive inputs to the OTAs. Again, leveraging the fact that the output of the OTA uses the bias voltage I_b as a gain, we can require one of the bias voltages to be α[T](V) and the other to be β. Setting β is straightforward since a current source can be fabricated out of a transistor connected to the OTA through a current mirror. To establish the presynaptic voltage dependence of the bias voltage for the other OTA in the gating variable computation requires additional circuitry, which will be described next.

The relationship between the presynaptic membrane voltage and the neurotransmitter concentration at the synaptic terminal very closely matches the output of a differential amplifier, as described in Liu, *et. al.* (2002). The differential amplifier is a circuit that, at its simplest, consists of just three transistors connected as in figure 17.

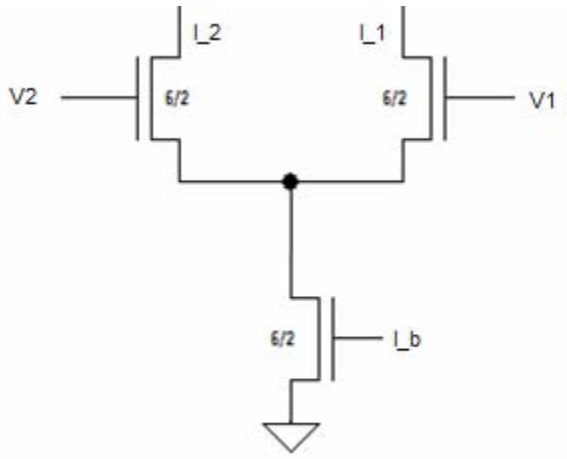

Figure 17. Simple differential amplifier

The output terminals I_1 and I_2 produce currents that are sigmoidal in shape and together sum to the bias current I_b. Specifically, the output of terminal I_1 is

$$I_1 = I_b \frac{1}{1+e^{\kappa_n (V_2 - V_1)/U_T}}. \quad (16)$$

There are two shortcomings in this circuit for implementing the dynamics of the transmitter concentration. The first is that there is no analogue to the k_p term, which sets the steepness of the

response curve independently of I_b (which changes the maximum value of I_1 and I_2. It turns out that the width of the linear regime for this device is set by properties of silicon devices that are difficult to control (e.g. the temperature). Thus, we accepted a rough approximation of the neurotransmitter voltage dependency for this model. The second shortcoming is that there is no intrinsic concept of $[T]_{max}$ in this circuit. However, this can easily be resolved by combining the $[T]_{max}$ with α in the bias current to the differential pair. It should be noted that the output from the differential pair is actually inverted from what would be expected. The output of the entire synapse corrects for this with an inverting amplifier that was added downstream.

One point that should be considered very carefully is that all of the circuits described above have narrow voltage ranges for which their behavior is as described. Thus, voltage signals need to be scaled to fit into the appropriate ranges for proper circuit operation. This is no trivial task, and many hours were spent adjusting parameters to get signals at each stage to be within reasonable bounds.

The final circuit for the entire synapse was assembled from the differential amplifier and OTA circuits as described above. The schematic for this circuit appears in figure 18. Several additional components have been added so that the main parts fit together. First, the input to the synapse required a buffer to reduce the voltage swing from the output of the neuron to fit with the required voltage ranges for the sbynapse. Second, the output of the neurotransmitter concentration circuitry (the differential pair) required a pair of current mirrors to maintain a high impedence input to the next stage of the synapse. Third, the output of the synapse required an amplifier to boost the output level to a range that was appropriate for activating the neuron. All three of these adjustments can be seen in figure 18.

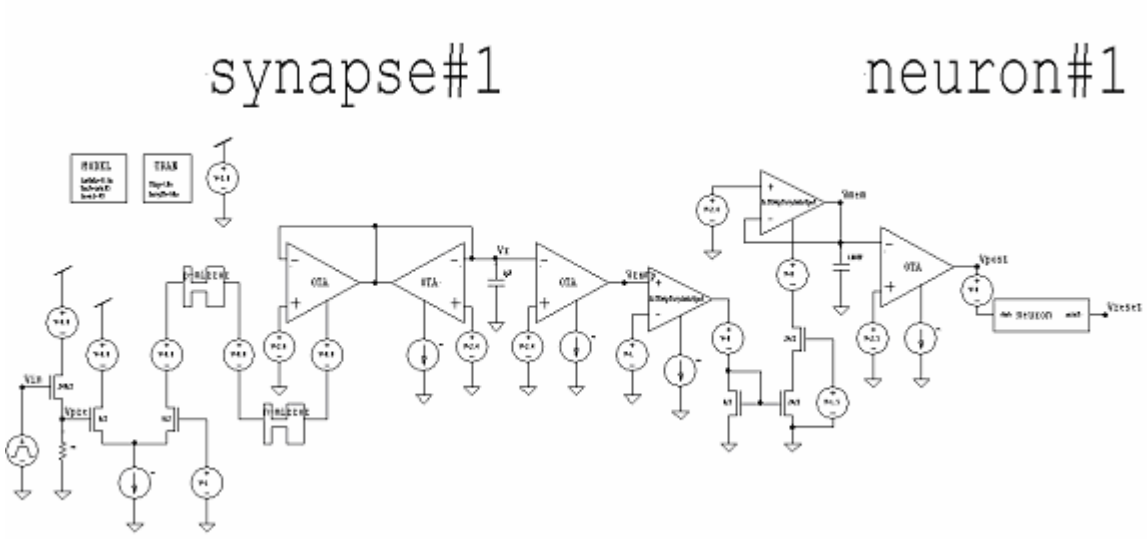

Figure 18. Schematic of the entire synapse. The output of this synapse is connected to the input of the integrate-and-fire neuron. Note the addition of voltage buffers, current mirrors, and amplifiers to the components already described.

Performance

In general, the circuitry performed quite well, and emulated the dynamics of a synapse closely. The performance of the two main components of the synapse (the circuit implementing the neurotransmitter concentration, and the circuit implementing the activation variable dynamics) as well as the performance of the entire circuit will be presented here.

Figure 19 compares the theoretical voltage dependence of the neurotransmitter concentration with that of our implementation. The primary difference is that we were unable to adjust the slope independently of the saturation voltages, and thus the shape isn't quite exact.

Figure 20 compares the theoretical activation variable dynamics to that of our implementation. Specifically, this figure compares the activation variable (r) response to a square wave input. Although the time constants do not match exactly, the fit is pretty close.

Figure 21 shows the output of the entire synapse, observed as a membrane voltage on a postsynaptic membrane. The wide duration of the post-synaptic potential is due to the addition of buffers to the neuron circuitry. This kept the firing frequency of the neuron at a reasonable rate, and contributed to the refractory period of the neuron. Aside from the shape of the postsynaptic action potentials, the output of the neuron performs reasonably well.

Figure 22 shows the schematic for our synapse connected to the IF neuron. A step voltage is applied to the synapse at the presynaptic node as the input.

Figure 23 shows the output of the cascaded synapse, observed as the membrane voltage on the first and second neurons. Notice that the pulse width of the spike decreased as the signal propagated from the first neuron to the second neuron.

Figure 24 shows the schematic for our cascaded synapse. This consists of a synapse connected to an IF neuron followed by a second synapse connected to a second IF neuron. A step voltage is applied to the first synapse at the presynaptic node as the input.

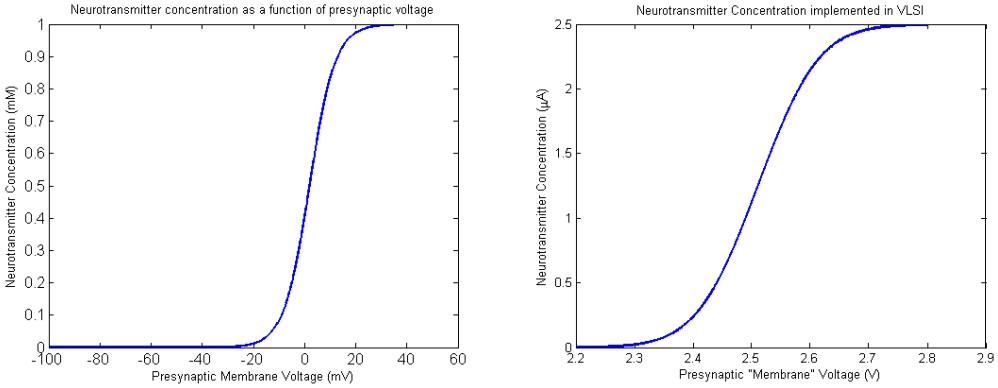

Figure 19. Comparison of the theoretical voltage dependence of the neurotransmitter concentration with that of the implementation. Note that the voltages have been remapped to fit appropriate ranges for the VLSI devices.

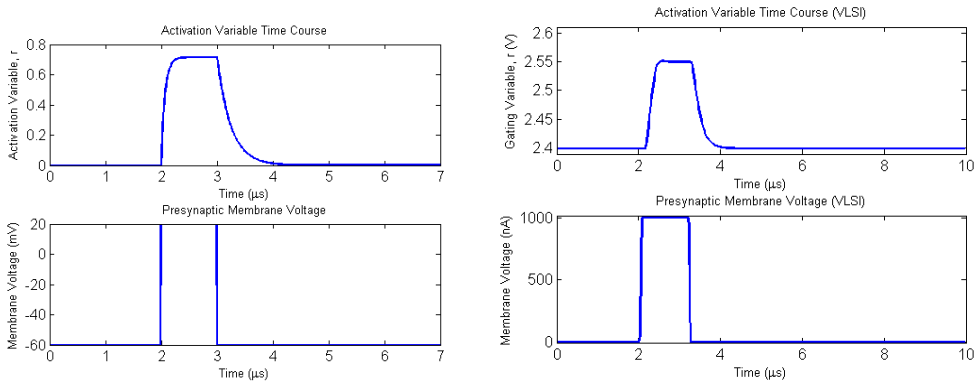

Figure 20. Comparison of the theoretical activation variable dynamics and that of the silicon implementation. Although the time constants do not match exactly, the fit is pretty close

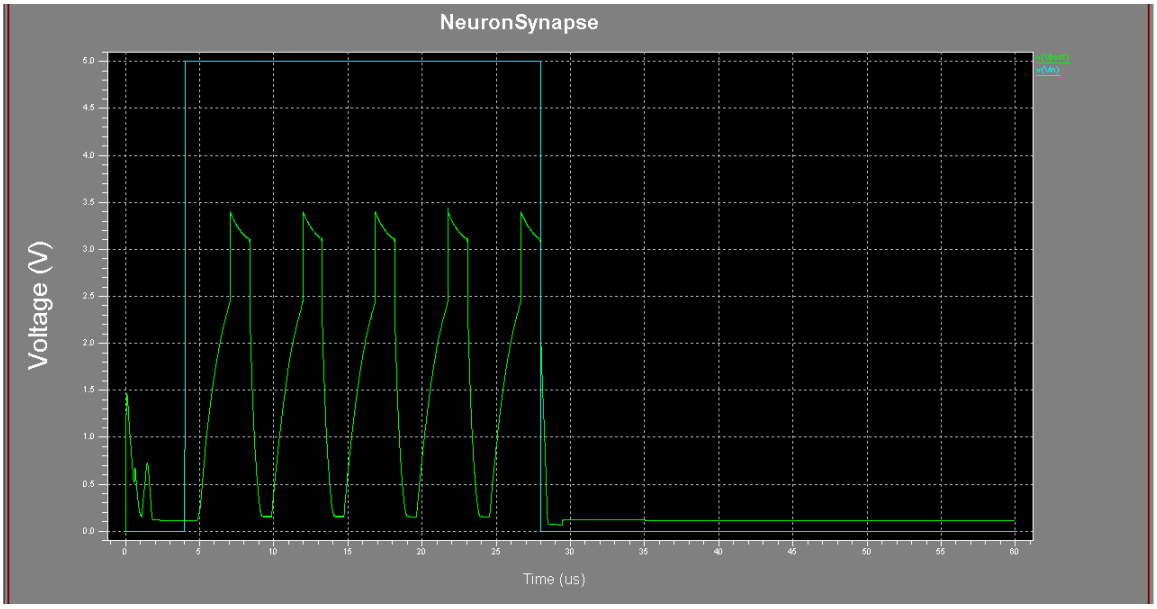

Figure 21. Response of synapse to a step input, observed as the membrane potential of the postsynaptic neuron. The output is shown in green and the input shown in blue.

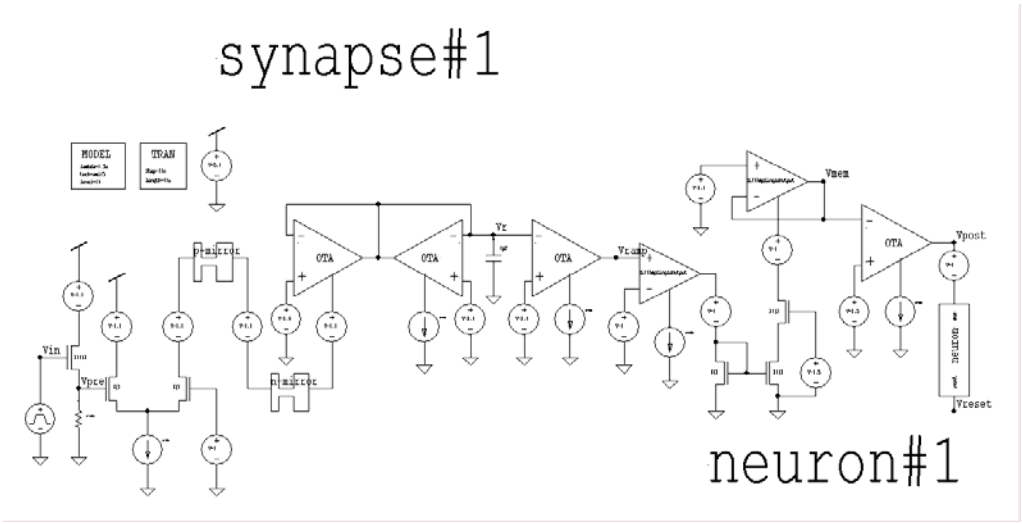

Figure 22. Schematic view of our IF neuron.

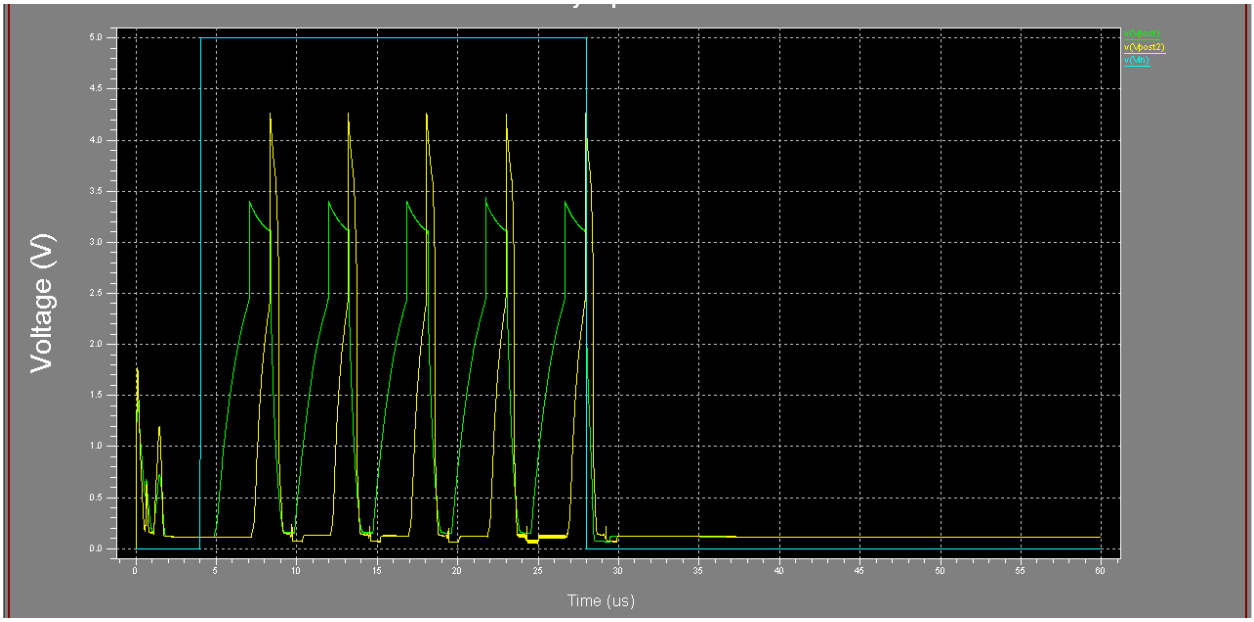

Figure 23. Response of a cascaded synapse to a step input, observed as the membrane potential of the postsynaptic neuron. The output of the first synapse is shown in green, the output of the second synapse is shown in yellow, and and the input shown in blue.

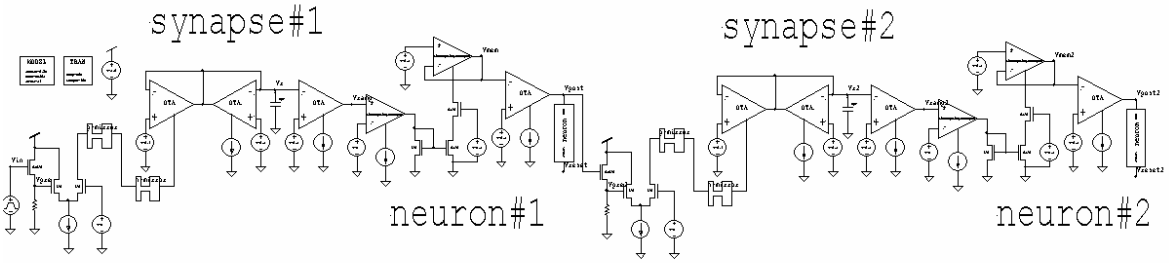

Figure 24. Schematic view of our cascaded synapse: synapse -> neuron -> synapse -> neuron

Reference List

(1) Destexhe A, Mainen ZF, Sejnowski TJ. An Efficient Method for Computing Synaptic Conductances Based on A Kinetic-Model of Receptor-Binding. Neural Computation 1994 Jan;6(1):14-8.

(2) Douglas R, Mahowald M, Mead C. Neuromorphic Analog Vlsi. Annual Review of Neuroscience 1995;18:255-81.

(3) Fragniere E, VanSchaik A, Vittoz EA. Design of an analogue VLSI model of an active cochlea. Analog Integrated Circuits and Signal Processing 1997 May;13(1-2):19-35.

(4) Harrison RR, Koch C. A robust analog VLSI motion sensor based on the visual system of the fly. Autonomous Robots 1999 Nov;7(3):211-24.

(5) Horiuchi T, Bair W, Bishofberger B, Moore A, Koch C, Lazzaro J. Computing Motion Using Analog Vlsi Vision Chips - An Experimental Comparison Among Different Approaches. International Journal of Computer Vision 1992 Sep;8(3):203-16.

(6) Kameda S, Yagi T. An analog VLSI chip emulating sustained and transient response channels of the vertebrate retina. Ieee Transactions on Neural Networks 2003 Sep;14(5):1405-12.

(7) Koch C, Mathur B. Neuromorphic vision chips. Ieee Spectrum 1996 May;33(5):38-&.

(8) Koch, C. Biophysics of Computation: Information Processing in Single Neurons, New York: Oxford University Press (1999).

(9) Kumar N, Himmelbauer W, Cauwenberghs G, Andreou AG. An analog VLSI chip with asynchronous interface for auditory feature extraction. Ieee Transactions on Circuits and Systems Ii-Analog and Digital Signal Processing 1998 May;45(5):600-6.

(10) Le Masson S, Laflaquiere A, Bal T, Le Masson G. Analog circuits for modeling biological neural networks: Design and applications. Ieee Transactions on Biomedical Engineering 1999 Jun;46(6):638-45.

(11) Lewis MA, Simo LS. Elegant stepping: A model of visually triggered gait adaptation. Connection Science 1999 Dec;11(3-4):331-44.

(12) Lewis MA, Bekey GA. Gait adaptation in a quadruped robot. Autonomous Robots 2002 May;12(3):301-12.

(13) Liu, S., et. al. Analog VLSI: Circuits and Principles, Cambridge, MA: MIT Press (2002).

(14) Lyon RF, Mead C. An Analog Electronic Cochlea. Ieee Transactions on Acoustics Speech and Signal Processing 1988 Jul;36(7):1119-34.

(15) Mahowald M, Douglas R. A Silicon Neuron. Nature 1991 Dec 19;354(6354):515-8.

(16) Mead, C. Analog VLSI and Neural Systems, Reading, MA: Addison-Wesley (1989).

(17) Morris C, Lecar H. Voltage Oscillations in the Barnacle Giant Muscle-Fiber. Biophysical Journal 1981;35(1):193-213.

(18) Rasche C, Douglas RJ. Silicon synaptic conductances. Journal of Computational Neuroscience 1999 Jul;7(1):33-9.

(19) Tenore F, Etienne-Cummings R, Lewis MA. ISCAS 2004 V349-V352.

(20) van Schaik A, Shamma S. A neuromorphic sound localizer for a smart MEMS system. Analog Integrated Circuits and Signal Processing 2004 Jun;39(3):267-73.

(21) Vandenberg CA, Bezanilla F. A Sodium-Channel Gating Model Based on Single Channel, Macroscopic Ionic, and Gating Currents in the Squid Giant-Axon. Biophysical Journal 1991 Dec;60(6):1511-33.

(22) Vogelstein RJ, Mallik U, Vogelstein JT, Cauwenberghs G. Dynamically reconfigurable silicon array of spiking neurons with conductance-based synapses. Ieee Transactions on Neural Networks 2007 Jan;18(1):253-65.